Acta Crystallographica Section B
Structural Science
ISSN 0108-7681

Complex disorder in β-$NH_4Fe_2(PO_4)_2$: deciphering from a five-dimensional formalism

Olivier Pérez,[a]* Laure Adam,[a] Anne Guesdon,[a] M. Daturi[b] and Bernard Raveau[a]

[a]Laboratoire CRISMAT, UMR 6508 CNRS, ENSICAEN 6 Boulevard du Maréchal Juin, 14050 Caen CEDEX, France, and [b]Laboratoire Catalyse et Spectrochimie, UMR 6506 CNRS, ENSICAEN 6 Boulevard du Maréchal Juin, 14050 Caen CEDEX, France

Correspondence e-mail: olivier.perez@ensicaen.fr

Received 12 December 2006
Accepted 2 May 2007

A new mixed-valent iron ammonium phosphate, β-$NH_4Fe_2(PO_4)_2$, has been synthesized. The diffuse scattering observed on the diffraction patterns implies complex disorder phenomena and prevents a direct structure resolution. The latter can be solved by generating an artificially ordered orthorhombic structure, using a five-dimensional approach and performing partial integration of the diffuse streaks. In the artificially ordered structure, hexagonal tunnels, delimited by FeO_6 octahedra, perpendicular to the directions [011] and $[0\bar{1}1]$ can then be seen; they are filled either by $[FeP_2O_{10}]_\infty$ zigzag ribbons or by NH_4^+ cations. It is shown that the disordering originates from the shifting of adjacent (100) tunnel slices of the structure with respect to each other along [011], allowing the formation of either new commensurate (superstructure) or incommensurate modulations, or even complete disorder along **a**. The close relationships with the ordered monoclinic form α-$NH_4Fe_2(PO_4)_2$ are also explained by this description.

1. Introduction

Iron phosphates represent a great potential for various applications, such as heterogeneous catalysis (Ai & Ohdan, 1997, 2000) or lithium storage electrodes for rechargeable batteries (Padhi *et al.*, 1997; Prosini *et al.*, 2002; Song *et al.*, 2002; Chung *et al.*, 2002). Besides, a large number of these materials are of great interest for their magnetic properties. This is the case for mixed-valent iron phosphates such as Fe_2PO_5, Fe_9PO_{12} and $Fe_7P_8O_{28}$, whose magnetic properties are closely related to ordering–disordering of the Fe^{2+} and Fe^{3+} species and to complex structural transitions (Modaressi *et al.*, 1981; Ijjaali *et al.*, 1990; Elkaïm *et al.*, 1996; Schmid-Beurmann, 2000).

Among the numerous iron phosphates that are actually known, those containing ammonium cations are of particular interest, since they are susceptible to being used as matrices to generate new phases in the 'Fe–P–O' system without foreign cations, by extracting the ammonium ion using soft chemistry methods or electrochemistry. The number of ammonium iron phosphates that are actually known is quite limited: three hydroxide iron phosphates – $Fe_2(NH_4)(OH)(PO_4)_2\cdot 2H_2O$ (Cavallec *et al.*, 1994), $FeNH_4HP_3O_{10}$ (Krasnikov *et al.*, 1983) and $NH_4H_8Fe_3(PO_4)_6\cdot 6H_2O$ (Moore & Araki, 1979) – and only one mixed-valent iron phosphate, $NH_4Fe_2(PO_4)_2$ (Boudin & Lii, 1998), have been synthesized to date. We have thus revisited the system 'NH_4–Fe–P–O' using hydrothermal synthesis. We have obtained a new form of the mixed-valent iron phosphate, that we name β-$NH_4Fe_2(PO_4)_2$, closely related to the form (named α) previously described by Boudin & Lii (1998). We show that the structure of this new β form, whose

doi:10.1107/S0108768107021647

diffraction patterns exhibit diffuse scattering, can be described as a disordered form, using a five-dimensional formalism to solve an artificially ordered structure.

Table 1
Experimental details.

Crystal data	
Chemical formula	$FeN_{0.5}O_4P$
M_r	157.8
Cell setting, space group	Orthorhombic, *Fddd*
Temperature (K)	173
a, b, c (Å)	17.152, 7.434, 10.05
V (Å^3)	1281.46
Z	16
D_x (Mg m^{-3})	3.271
Radiation type	Mo $K\alpha$
μ (mm^{-1})	5.04
Crystal form, colour	Needle, black
Crystal size (mm)	0.2 × 0.04 × 0.04
Data collection	
Diffractometer	Nonius CCD
Data collection method	See text
Absorption correction	None
No. of measured, independent and observed reflections	29 264, 5543, 2625
Criterion for observed reflections	$I > 3\sigma(I)$
$R_{\rm int}$	0.099
$\theta_{\rm max}$ (°)	42.0
Refinement	
Refinement on	F
$R[F^2 > 2\sigma(F^2)]$, $wR(F^2)$, S	0.051, 0.041, 1.67
No. of reflections	5543
No. of parameters	106
Weighting scheme	Based on measured s.u.s, $w = 1/\sigma^2(F)$
$(\Delta/\sigma)_{\rm max}$	0.001
$\Delta\rho_{\rm max}$, $\Delta\rho_{\rm min}$ (e Å^{-3})	2.87, −2.64
Extinction method	B-C type 1 Gaussian isotropic (Becker & Coppens, 1974)
Extinction coefficient	0.014 (7)

Computer programs: *JANA*2000 (Petricek & Dusek, 2000).

2. Synthesis

The single crystal used for the structure determination of β-$NH_4Fe_2(PO_4)_2$ was extracted from a batch prepared under hydrothermal conditions in the following way. A mixture of Ga_2O_3, $FeCl_2$, Fe_2O_3 and $(NH_4)H_2PO_4$, in the respective molar ratio 0.5:1:0.5:3, was placed in a 21 ml Teflon-lined stainless steel autoclave with 2 ml of deionized water (pH of the as-prepared solution ~ 2). It was heated at 493 K over 40 h and then cooled to room temperature. After cooling, the solid products were collected by filtration of the final solution (pH $\simeq$ 2), washed with deionized water and dried in air. Examination of the resulting pinkish powder revealed the presence of a mixture of red, white and pink powders containing black streaked crystals of the title compound.

A single-phase sample of β-$NH_4Fe_2(PO_4)_2$ was synthesized starting from a mixture of Fe_2O_3, $FeCl_2$ and $(NH_4)_2HPO_4$, in the respective ratio 0.25:0.5:1, placed with 2 cm^3 of deionized water in a 21 ml Teflon-lined stainless steel autoclave. It was heated at 493 K over 25 h and then cooled to 298 K for 17 h. The resulting product was filtered and washed with deionized water, leading to the black powder of the title compound.

3. Semiquantitative analysis

Semi-quantitative analyses of some black crystals extracted from the preparation were performed with an OXFORD 6650 microprobe mounted on a PHILIPS XL30 FEG scanning electron microscope. They revealed the presence of Fe and P elements in the approximate ratio 1:1 in the crystals, in agreement with the composition deduced from the single-crystal X-ray diffraction study.

4. IR analysis

The IR spectra of the self-supported sample was recorded in the region 4000–650 cm^{-1}, using a Thermo-Electron Nicolet 5700 Fourier-transform instrument equipped with an extended KBr beam splitter and with an MCT cryo-detector.

Material properties were studied by *in situ* FT-IR spectroscopy of adsorbed probe molecules, using sample wafers of 10 mg cm^{-2} analysed in a classical quartz cell connected to a vacuum glass line. Spectra were recorded (resolution 4 cm^{-1}) after quenching the samples to room temperature. Probe molecules were introduced at room temperature on the activated sample and then evacuated. The spectra were treated by the Nicolet OMNI™ software.

5. Data collection, symmetry and refinement

5.1. Data collection

The experimental details are summarized in Table 1. A preliminary X-ray diffraction investigation was performed on single crystals at room temperature, using Mo $K\alpha$ radiations on a Kappa CCD (Bruker Nonius) diffractometer.[1] Large Ω and χ scans were used to measure the crystalline quality of different crystals and to determine the cell parameters. It can be noted that for all the samples some frames exhibit diffuse diffraction lines. One single crystal of suitable size (~ 0.2 × 0.04 × 0.04 mm^3) was then selected.

Considering the cell parameters and the size of the spot, suitable data collection strategies were defined. Room-temperature measurement was performed using a scanning angle of 0.5° and a D_x (detector–sample distance) value of 34 mm; Φ and Ω scans were chosen. Two different exposure times (200 and 6 s per °) were used during the data collection in order to collect a maximum number of reflections, but avoiding any detector saturation by reflections of strong intensity. The diffracted intensities were collected up to $\theta = 42°$ ($0 \le h \le 34$, $0 \le k \le 14$ and $0 \le l \le 20$). Plots of reciprocal lattice planes assembled from these series of experimental frames are sufficiently accurate to obtain an overall view of the reciprocal space. The diffraction pattern (Figs. 1*a* and *b*)

---

[1] Supplementary data for this paper are available from the IUCr electronic archives (Reference: CK5023). Services for accessing these data are described at the back of the journal.

can be described within an orthorhombic cell [cell parameters a = 17.1491 (2), b = 7.4419 (2), c = 10.0522 (3) Å]. The observed conditions limiting the possible reflections, hkl: $h + k = 2n, h + l = 2n, k + l = 2n$, $0kl$: $k + l = 4n$, $k, l = 2n$, $h0l$: $h + l = 4n$, $h, l = 2n$, $hk0$: $h + k = 4n$, $h, k = 2n$, $h00$: $h = 4n$, $0k0$: $k = 4n$ and $00l$: $l = 4n$ are consistent with the space group *Fddd*. However, extra diffraction spots of weak intensity are observed on the ($0kl$), ($1kl$), ($2kl$)… diffraction planes (Fig. 2*a*). Each intense Bragg reflection (so-called main reflection) is surrounded by four of these extra spots; they can be connected to the main reflections *via* the vectors $\mathbf{q}_1^* = 0.5\mathbf{b}^* + 0.5\mathbf{c}^*$, $\mathbf{q}_2^* = 0.5\mathbf{b}^* - 0.5\mathbf{c}^*$, $-q_1^*$ and $-q_2^*$. The observation of the ($h\frac{1}{2}l$) or ($hk\frac{1}{2}$) planes (Fig. 2*b*) reveals the true nature of this diffraction phenomenon. The extra spots observed on the ($0kl$) planes correspond to the intersection of diffuse scattering lines. The existence of this diffuse scattering can be related to planar disorder: it can be interpreted by the existence of additional periodicities in the (bc) plane but with a loss of correlation along **a**.

To change this particular diffuse scattering phenomenon, either by a modification of the position of the lines (change of the partial order) or by a condensation of the lines into point reflections (generation of a total ordering), measurement was performed at 173 K. Except for the use of the Oxford cryosystem, frames were collected with the strategy already detailed for the room-temperature data collection. No change was observed on the diffraction patterns; the diffuse lines appear at the same position and with the same intensities.

5.2. Structure determination and refinement

The *EvalCCD* software (Duisenberg *et al.*, 2003) was used to extract reflections from the collected frames; reflections were merged and rescaled as a function of the exposure time. Data were corrected for absorption using the *SADABS* program (Sheldrick, 1997) developed for the scaling and correction of area-detector data. A structural model considering the *Fddd* space group was built up with *SIR*2002 (Burla *et al.*, 2002) using direct methods both using room-temperature and 173 K data sets. 898 and 883 reflections with $I \geq 3\sigma(I)$ were extracted at 173 K and room temperature, respectively. Two Fe, one P and the three O atoms were located. This model was then introduced into the refinement program *JANA*2000 (Petricek & Dusek, 2000); all the atomic positions were

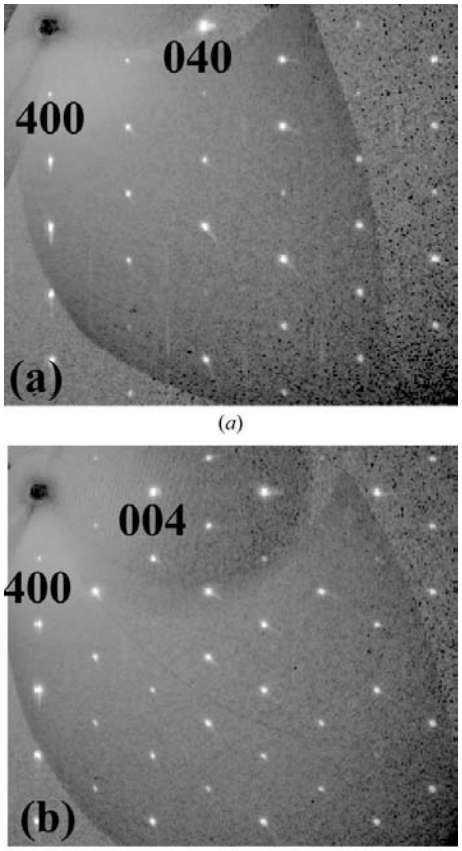

(*a*)

(*b*)

Figure 1
(*a*) ($hk0$) and ($h0l$) diffraction planes calculated from experimental frames. Indices are given in the average cell a = 17.1491 (2), b = 7.4419 (2), c = 10.0522 (3) Å.

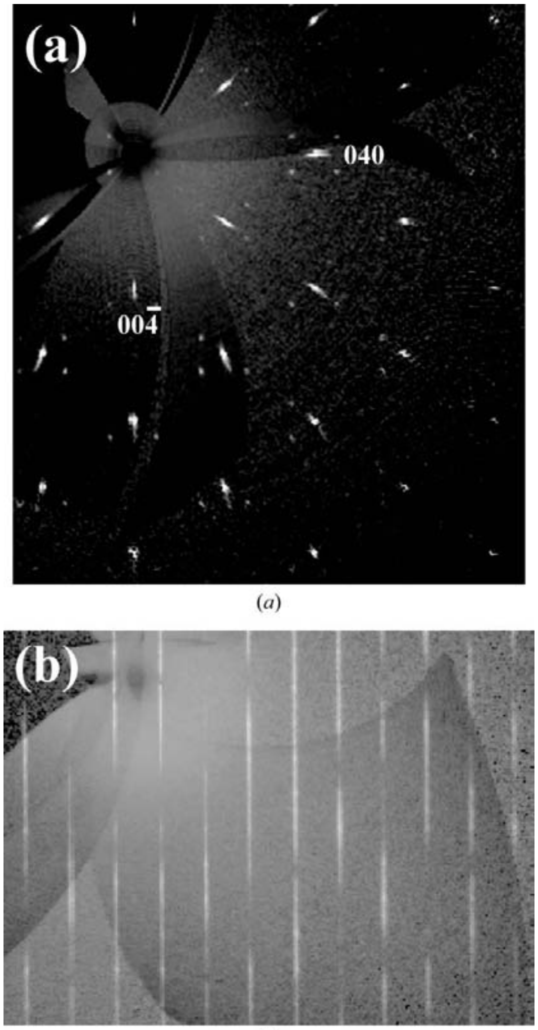

(*a*)

(*b*)

Figure 2
(*a*) ($0kl$) and (*b*) ($h\frac{1}{2}l$) diffraction planes calculated from experimental frames. Indices are given in the average cell a = 17.1491 (2), b = 7.4419 (2), c = 10.0522 (3) Å.

Table 2
Positional parameters and ADP harmonic parameters (Å^2).

	Occupancy	x	y	z	$U_{\rm iso}$ (Å^2)
Fe1	1	0	0	0.5	0.00509 (6)
Fe2	0.4886 (12)	0.153522 (18)	0	0	0.00383 (9)
N	0.5114 (12)	0.0863 (2)	0	0	0.0243 (9)
P	0.5	0.06078 (2)	0.79881 (7)	0.22655 (5)	0.00369 (9)
O1	0.5	0.11587 (6)	0.0550 (2)	0.48651 (15)	0.0057 (3)
O2	1	0.00800 (4)	0.68836 (14)	0.13945 (11)	0.0171 (2)
O3	0.5	0.08497 (7)	0.9825 (2)	0.16789 (16)	0.0080 (3)

	U^{11}	U^{22}	U^{33}	U^{12}	U^{13}	U^{23}
Fe1	0.00326 (9)	0.00893 (13)	0.00310 (10)	0	0	0
Fe2	0.00299 (13)	0.00462 (16)	0.00387 (16)	0	0	−0.00104 (12)
N	0.0303 (14)	0.0230 (18)	0.0197 (15)	0	0	0.0106 (14)
P	0.00350 (13)	0.00404 (18)	0.00352 (16)	−0.00049 (12)	−0.00002 (11)	−0.00010 (13)
O1	0.0034 (4)	0.0071 (5)	0.0067 (5)	0.0002 (4)	−0.0006 (3)	0.0000 (5)
O2	0.0064 (2)	0.0142 (4)	0.0306 (5)	0.0037 (2)	−0.0081 (3)	−0.0156 (4)
O3	0.0084 (4)	0.0061 (7)	0.0096 (6)	−0.0027 (4)	0.0002 (4)	0.0021 (5)

refined and then anisotropic displacement parameters (ADP) were considered for all the atoms. The refinement led to an agreement factor equal to 5.5%. Fe2, P, O1 and O3 exhibit an occupancy of $\frac{1}{2}$. Moreover, P and O1 are split over two equivalent positions by the symmetry operators (i) $\frac{1}{4}-x, -y, \frac{1}{4}-z$ and (ii) $x, -y, 1-z$, respectively; dP—P$^{\rm i}$ = 0.8654 (7) and dO1—O1$^{\rm ii}$ = 0.861 (2) Å. These split positions as well as the statistical occupancies can be correlated to the diffuse scattering observed on the experimental frames. A difference-Fourier synthesis was then calculated. The maximum positive peak $M1$ was located at the coordinates (0.086; 0; 0) with density ρ = 9 e Å^{-3}; the $M1$—Fe2 distance is equal to 1.16 Å. This too-short distance correlated to the statistical occupancy observed for Fe2 implies a statistical occupancy for $M1$. Considering the different elements introduced during the synthesis, the $M1$ site could be occupied either by $\frac{1}{2}\,H_2O, \frac{1}{2}\,H_3O^+$ or $\frac{1}{2}\,NH_4^+$. In order to determine which species was located on the $M1$ site, IR analysis was performed. The IR spectrum of the self-supported sample was recorded after evacuation at 2.4 × 10^{-3} Pa. A large absorption in the region 3400–2700 cm^{-1}, typical of a complex containing ν(NH) stretching modes (Zecchina *et al.*, 1997), shows the presence of coordinated ammonium species, as already discussed by Bonhomme *et al.* (2002). The corresponding δ(NH) bendings are contained in the peak centred near 1450 cm^{-1}. Features between 2200 and 1600 cm^{-1} are due to overtones and combinations of the structural bands (essentially assigned to phosphate groups) absorbing in the region 1250–700 cm^{-1} (Daturi *et al.*, 2001). A more detailed study of all these modes, as well as an investigation on the skeletal bands at lower wavenumbers, will require an analysis of the sample diluted in KBr. However, since these analyses have shown the presence of coordinated ammonium cations, an N atom has been located on the $M1$ site. Owing to the short Fe2—N distance, the sum of N and Fe2 site occupancies had to be constrained to be equal to one. The final agreement factor reached 2.5% for 898 independent reflections [with $I \geq 3\sigma(I)$]. Refinement results obtained for the data colleted at 173 K are reported in Table 2. Fourier-difference synthesis finally led to the residue −0.5 e Å^{-3}.

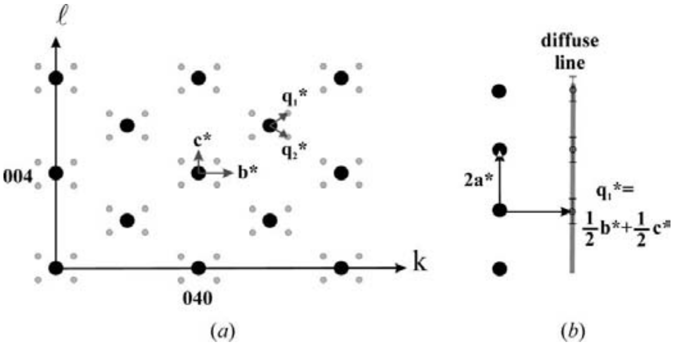

Figure 3
Drawings providing a clarified view of the (0kl) plane and in particular of the diffuse lines; the choice of the wavevectors is justified and the length of the integration boxes used to integrate the 'pseudo reflections' is depicted.

5.3. An artificial order

The previous refinement is based only on the main reflections. Numerous atoms are affected by a stochastic disorder and then the description of the structure is not trivial. To simplify the structural analysis, an ordered model is necessary. The observation of the diffuse scattering (Fig. 2), known to be associated with the existence of a partial order, allows us to imagine the possibility of generating such a model. The information about disorder being mainly condensed in the diffuse scattering, a partial integration of the diffuse lines was realised. As shown in Fig. 3, nodes of the diffraction pattern were defined using the simplest $\mathbf{q}_1^*$ and $\mathbf{q}_2^*$ vectors, but with respect to the lattice translation; no component along **a*** was considered. For all streaks, boxes elongated along **a*** (a length of 0.3**a*** has been used) were chosen to retrieve the maximum intensity of the diffuse lines into these 'pseudo reflections', but avoiding overlapping of the different nodes. Using the main reflections, as well as those pseudo reflections, an artificially ordered structure could be generated. However, as it was not possible to collect all the diffuse intensity, an additional scale factor was introduced in our data set for the 'pseudo reflections'; this new parameter should compensate for the loss of intensity owing to the extraction process.

Two hypotheses can be used for both data extraction and refinement. The first hypothesis is based on a classical supercell (a,2b,2c) description. The main and the pseudo reflections are located at the nodes of a classical reciprocal space. Figs. 2 and 3 show the limit of this hypothesis. The majority of the nodes are extinct. As a consequence, the number of observed 'pseudo reflections' is very limited. This limitation of the resulting data set, combined with the large number of independent atoms to consider in the supercell, induces a lot of correlations between the refinement parameters. The expected results in such an approach is finally of weak interest. A second hypothesis is based on superspace formalism (Janssen *et al.*, 1999; de Wolff *et al.*, 1981), developed for aperiodic structures. In this formalism, the introduction of extra dimensions allows the building of a totally periodic supercrystal in a space of higher dimension: the superspace. The main reflections are located using the three vectors $\mathbf{a}^*$, $\mathbf{b}^*$ and $\mathbf{c}^*$ and are indexed $hk\ell00$. The 'pseudo reflections' resulting from the integration of the diffuse lines require five vectors ($\mathbf{a}^*$, $\mathbf{b}^*$, $\mathbf{c}^*$, $\mathbf{q}_1^* = \frac{1}{2}\mathbf{b}^* + \frac{1}{2}\mathbf{c}^*$, $\mathbf{q}_2^* = \frac{1}{2}\mathbf{b}^* - \frac{1}{2}$); they are called satellite reflections and are indexed $hklmn$ with $m \neq 0$ and/or $n \neq 0$. Considering that both main and satellite reflections are compatible with the F-centring lattice (as observed in the diffraction planes in Figs. 1 and 2), the extraction of data from the experimental frames is considerably simplified compared with the previous hypothesis. Moreover, in such an approach, the structure is considered as resulting from the perturbation of an average structure [corresponding to the model previously refined in the (a, b, c) sub cell]; the perturbation corresponds to a modulation affecting some parameters. Owing to the real nature of the artificial satellite reflections (diffuse lines), no extra condition limiting the possible reflections in the five-dimensional approach is observed. The artificial diffraction pattern is then consistent with the superspace group *Fddd*(0*pq*,0*p*–*q*).

Using only satellite reflections, a starting superspace model was determined applying a modulation of occupancy to the Fe2, N, P, O1 and O3 atoms of the model summarized in Table 2. To generate a completely ordered model, the occupancy of the Fe2, N, P, O1 and O3 atoms should be described by crenel functions. The sites would exhibit full and null occupancies *versus* $\bar{x}_4$ and $\bar{x}_5$ (coordinate along the two additional dimensions). However, this type of function is not implemented for the five-dimensional approach in *JANA*2000 (Petricek & Dusek, 2000). The occupancy was then expanded using Fourier series. Since only first-order satellite reflections ($\pm\mathbf{q}_1^*$, $\pm\mathbf{q}_2^*$) were observed, the harmonics used were developed up to first order

$$P(\bar{x}_4, \bar{x}_5) = P_0 + A_1 \sin 2\pi\bar{x}_4 + B_1 \cos 2\pi\bar{x}_4 + A_2 \sin 2\pi\bar{x}_5 + B_2 \cos 2\pi\bar{x}_5. \quad (1)$$

The amplitudes A_1, B_1, A_2, B_2 were firstly defined in order to obtain functions as close as possible to crenel shape functions. Since $\mathbf{q}_1^* \pm \mathbf{q}_2^*$ reflections were not observed, mixed second-order Fourier terms were not introduced. The sign of A_i and B_i was then tested *via* a trial-and-error method. Once this first model was established, the artificial satellite reflections could be used. To take into account the complementary occupancy of the Fe2 and N sites, a modulation of substitution was introduced. The sum of occupancy for these two atoms was then fixed to one. The modulation functions are highly significant for Fe2, N, P, O1 and O3, outlining the primary role of the modulation of occupancy in the structure. The reliability factor for the satellite reflections reached 27%. At this step of the refinement, a displacive modulation was introduced for the whole atoms. Each atom is thus described with an average position r_0 and a displacement U; this displacement is expanded using Fourier series

$$U(\bar{x}_4, \bar{x}_5) = A_1 \sin 2\pi\bar{x}_4 + B_1 \cos 2\pi\bar{x}_4 + A_2 \sin 2\pi\bar{x}_5 + B_2 \cos 2\pi\bar{x}_5. \quad (2)$$

The refinement of the displacement parameters led to Fourier terms of weak amplitude. This modulation is considered as a secondary effect; the occupancy modulation being the driving force of the structure ordering.

Crystallographic analysis based on the superspace formalism provides the structure of a supercrystal in a space of higher dimension; the actual structure of the crystal corresponds to a section of the supercrystal by the physical space. The section is defined at fixed t and u values, t and u referring to the coordinates along the fourth and the fifth dimensions, respectively. For an incommensurate phase, owing to the irrational value of the wavevectors, all the sections of the supercrystal are equivalent. For a commensurate phase, only some sections have a physical meaning and then the choice of the origin (t_0, u_0) becomes crucial. Analysis of the possible sections and of their symmetry, compatible with the superspace group *Fddd*(0*pq*,0*p*–*q*), leads for the supercell $(a, 2b, 2c)$ to the following choice

$$t_0 = 0,\ u_0 = 0: \quad \text{space groups } A222,$$
$$t_0 = 0,\ u_0 = 1/8: \quad \text{space groups } A\bar{1},$$
$$t_0 = 1/8,\ u_0 = 1/8: \quad \text{space groups } A2_122.$$

These different sections were tested. The best result was obtained for (t_0 = 1/8, u_0 = 1/8) leading to the space group

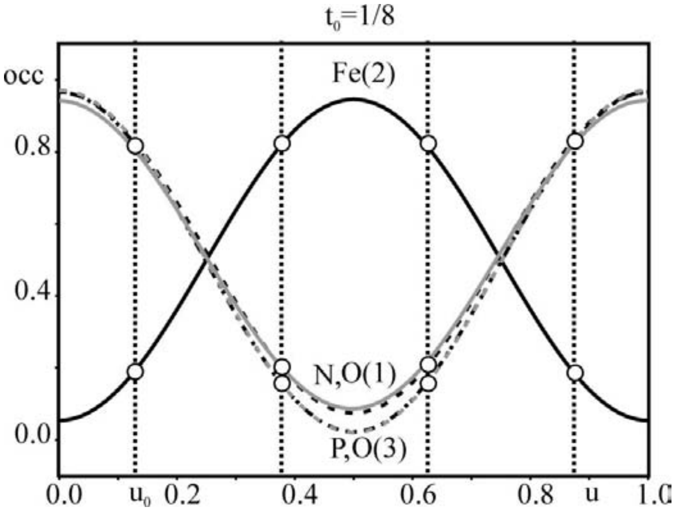

Figure 4
Site occupancy as a function of u and at t_0 = 1/8. Vertical dashed lines are guides to the eyes: they help the reader to find the physical points (white circles) implied by the section choice and as required to build the structure in the supercell.

Table 3
Positional and occupancy parameters for the artificially ordered structure.

		x	y	z	Occupancy
Fe1	<>	0	0	0.5	1
	A_1	0	−0.00678 (10)	−0.00049 (5)	
	B_1	0.00053 (2)	0	0	
	A_2	0	−0.00678 (10)	0.00049 (5)	
	B_2	−0.00053 (2)	0	0	
Fe2	<>	0.15347 (4)	0	0	0.5
	A_1	0	−0.00400 (14)	0.00228 (10)	0
	B_1	−0.00098 (4)	0	0	0
	A_2	0	−0.00170 (14)	0.00074 (10)	0
	B_2	−0.00016 (8)	0	0	−0.446 (5)
N	<>	0.08617 (14)	0	0	0.5
	A_1	0	−0.0050 (12)	0.0017 (9)	0
	B_1	0.0031 (4)	0	0	0
	A_2	0	0	0	0
	B_2	0	0	0	0.446 (5)
P	<>	0.060803 (18)	0.79906 (17)	0.22640 (12)	0.5
	A_1	−0.00025 (5)	−0.00025 (17)	0.00053 (12)	0.004 (2)
	B_1	−0.00142 (5)	0.00193 (17)	0.00028 (11)	0.0053 (18)
	A_2	0	−0.0009 (3)	0.0005 (2)	0.459 (6)
	B_2	−0.00012 (5)	−0.00066 (18)	0.00035 (12)	−0.107 (2)
O1	<>	0.11607 (12)	0.0552 (4)	0.4859 (3)	0.5
	A_1	0.00040 (16)	0	0	0.015 (6)
	B_1	0.00076 (13)	−0.0026 (5)	0.0009 (4)	0
	A_2	0.0003 (2)	0.0012 (8)	−0.0012 (6)	−0.420 (7)
	B_2	0	0.0007 (5)	0	0.085 (5)
O2	<>	0.00798 (3)	0.68834 (10)	0.13927 (8)	1
	A_1	−0.00047 (8)	−0.0022 (3)	0.0016 (2)	
	B_1	0.00034 (8)	0.0034 (3)	−0.0026 (2)	
	A_2	0.00225 (8)	0.0096 (3)	−0.0154 (2)	
	B_2	−0.00043 (8)	−0.0018 (3)	0.0017 (3)	
O3	<>	0.08511 (8)	0.9797 (6)	0.1684 (3)	0.5
	A_1	−0.00176 (16)	0.0028 (5)	0.0019 (4)	0.009 (5)
	B_1	−0.00247 (16)	0.0046 (5)	0.0011 (4)	0
	A_2	−0.00037 (18)	0.0019 (7)	0	0.263 (6)
	B_2	0	−0.0053 (9)	0.0012 (5)	−0.396 (7)

$A2_122$ for the supercell (a, $2b$, $2\mathbf{c}$). Fig. 4 shows the evolution of the occupancy of Fe2, N, P, O1 and O3 at $t_0 = 1/8$ *versus* u; it clearly shows an ordering between the different atomic sites. Considering a 0.2 cut-off for the occupancies, our model allows the generation of atomic vacancies or fully occupied sites depending on (t, u). The final reliability factor is 2.6% for 898 independent main reflections and 9.4% for 1727 independent satellites [with $I \geq 3\sigma(I)$]. Refined atomic parameters are listed in Table 3. During the refinement strategy, two independent scale factors were introduced for main and satellite reflections. The scale factor refined for the 'pseudo reflections' corresponds to 70% of one of the main reflections. This parameter then induces an artificial increase in the intensity of the satellites and by correlation a magnification of the modulation amplitudes. However, this magnification is rather helpful since the goal of the present refinement is to generate a completely ordered model.

6. Structural description

6.1. The real structure

The refinement in the real structure reveals the existence of an important disorder phenomenon in β-$NH_4Fe_2(PO_4)_2$. The model obtained is indeed built up from two fully occupied atomic sites, Fe1 and O2, and five statistically occupied sites, Fe2, N, P, O1 and O3 (Table 2*a*). The understanding of the structure of β-$NH_4Fe_2(PO_4)_2$ implies an accurate analysis of the resulting disorder. As a matter of fact, this model leads for

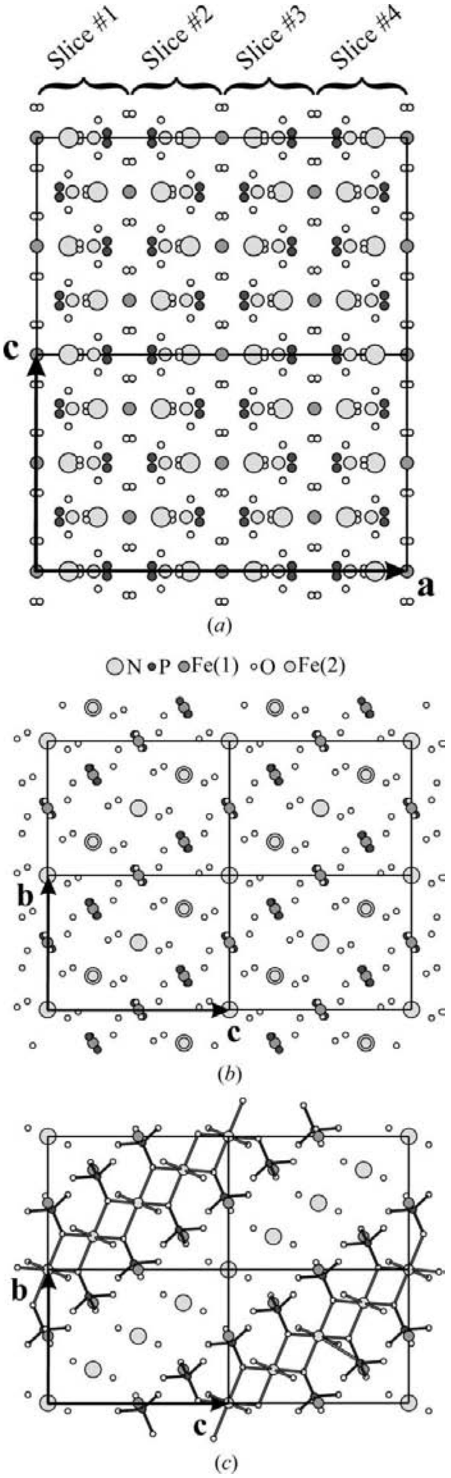

Figure 5
Projection of the real structure of β-$NH_4Fe_2(PO_4)_2$ along **b** (*a*) and along *a* (**b**). The projection along **a** of a possible configuration for the slice #1 defined in Fig. 4(*a*) is shown in Fig. 4(*c*), with the bonding scheme of Fe2 and P.

Table 4
Positional parameters in the (*a* 2*b* 2*c*) supercell (space group: $A2_122$).

	x	*y*	*z*		*x*	*y*	*z*
Fe1–1	−0.0008	0.125	0.2497	O1–6	0.8651	0.7783	0.132
Fe1–2	0.2492	0.2452	−0.125	O1–7	0.6166	0.9011	0.2437
Fe1–3	0	0.3798	0.5	O1–8	0.8667	0.0268	−0.1185
Fe1–4	0	0.8702	0.5	O2–1	0.0094	0.4713	0.0655
Fe1–5	0.25	0.5	0.1253	O2–2	0.0065	0.967	0.0738
Fe1–6	0.25	0	0.1247	O2–3	0.2562	0.5894	0.0486
Fe2–1	0.1543	0.627	−0.0011	O2–4	0.2598	0.0989	0.0622
Fe2–2	0.4029	0.248	0.1239	O2–5	0.0099	0.7241	0.3133
Fe2–3	0.1529	0.8742	0.2505	O2–6	0.0061	0.2142	0.326
Fe2–4	0.4043	0.0008	0.3755	O2–7	0.2593	0.8461	0.31
P1	0.062	0.524	0.1129	O2–8	0.2566	0.3422	0.3007
P2	0.3096	0.1495	0.0112	O2–9	0.5101	0.474	0.3128
P3	0.0598	0.7751	0.3635	O2–10	0.5059	0.9643	0.3264
P4	0.3119	0.8984	0.2618	O2–11	0.7558	0.5892	0.299
P5	0.5598	0.5248	0.3634	O2–12	0.7602	0.0992	0.3117
P6	0.81	0.1504	0.2619	O2–13	0.5069	0.7173	0.0743
P7	0.5617	0.2732	0.1136	O2–14	0.509	0.221	0.065
P8	0.8118	0.3988	0.0118	O2–15	0.7568	0.8421	0.0512
N1	0.0884	0.1232	0.0006	O2–16	0.7591	0.3462	0.0595
N2	0.334	0.7518	0.1256	O3–1	0.0876	0.6152	0.0826
N3	0.084	0.3768	0.2494	O3–2	0.3323	0.2434	0.0398
N4	0.3384	0.4982	0.3744	O3–3	0.0827	0.8693	0.3347
O1–1	0.1155	0.1536	0.2429	O3–4	0.3372	0.9893	0.292
O1–2	0.3662	0.7759	−0.1188	O3–5	0.583	0.6181	0.3344
O1–3	0.1163	0.4015	0.4936	O3–6	0.8334	0.244	0.2911
O1–4	0.3654	0.5279	0.1319	O3–7	0.5865	0.3646	0.0838
O1–5	0.615	0.1526	0.4932	O3–8	0.837	0.4905	0.0416

instance to eight oxygen neighbors for Fe atoms: four half-occupied O1 and four fully occupied O2 for Fe1, and two half-occupied O1, one fully occupied O2 and four half-occupied O3 for Fe2 (Figs. 5*a* and *b*). However, examination of the cationic environments (O3 only linked to Fe2 and P) and of the atomic distances ($d\text{Fe2—N} < 1.2$ Å, $d\text{P—P}$ and $d\text{O1—O1} < 0.9$ Å) leads to some rules which allow a better understanding of the structure. Simple models can thus be built by considering the elementary cell (*a*, *b*, *c*) as a stacking along **a** of four slices of equal thickness (Fig. 5*a*). The projection of one of these (2*b*, 2*c*) slices along **a** is given on Fig. 5(*b*). Since the Fe2—N distance is smaller than 1.2 Å, these two atoms (which are both located on half-occupied crystallographic sites) cannot coexist. If we consider the hypothesis that the (0.15; 0; 0) site is not occupied by Fe2 and thus that the N atom fully occupies the (0.09; 0; 0) site, then the O3 first neighbor has to be removed because, otherwise, there would be a too-short N—O3 distance (about 1.69 Å). As a consequence, the nearest P atom cannot be present since its presence is correlated to the presence of O3, which takes part of its tetrahedral coordination. In a similar way, the analysis of the oxygen environment of the two closest P atoms along the [011] direction rules out the O1 site, which exhibits a too-short P—O1 distance (1.26 Å). Environment considerations along the $[0\bar{1}1]$ direction allow the two Fe2 neighbors to be removed. Thus, gradually, it is possible to generate an ordered structural slice (Fig. 5*c*). In this ordered slice, P exhibits a regular tetrahedral environment with $1.50 < d\text{F—O} < 1.63$ Å, Fe1 and Fe2 an octahedral environment with $1.98 < d\text{Fe1—O} < 2.04$ Å and $2.06 < d_{\text{Fe2—O}} < 2.16$ Å.

Different possible configurations can then be isolated for one slice, but it is not easy to imagine the stacking of the slices along **a**. The disorder prevents a global description of the structure.

6.2. The artificially ordered structure

The structural refinement performed in the (*a* 2*b* 2*c*) supercell provides an artificially ordered structure for β-$NH_4Fe_2(PO_4)_2$. The corresponding atomic positions generated from the superspace approach (Table 3) are listed in Table 4. The atoms labelled Fe1–1, ... Fe1–#, Fe2–1, ... Fe2–#, O1–1, ... O1–#, O2–1, ... O2–# and O3–1, ... O3–# are generated from Fe1, Fe2, O1, O2 and O3, respectively. The oxygen environment of P and Fe atoms is summarized in Table 5. The structure consists of a three-dimensional mixed framework built from PO_4 tetrahedra and FeO_6 octahedra (Figs. 6*a* and *b*); the projections along [011] (Fig. 6*b*) and $[0\bar{1}1]$ are equivalent. These polyhedra share apices and edges, forming hexagonal tunnels running along the [011] and $[0\bar{1}1]$ directions and containing the ammonium cations. The PO_4 tetrahedra are isolated, *i.e.* only linked to FeO_6 octahedra. They present regular geometries, with P—O distances ranging from 1.51 to 1.57 Å (Table 5), *i.e.* similar to the distances usually observed for monophosphate groups. The bond-valence calculations (BVS) lead to an oxidation state close to 5 (~ 4.92–4.96) for the P atoms. Two types of FeO_6 polyhedra are shown in the structure. Iron atoms labelled Fe1 exhibit Fe—O distances ranging from 1.94 to 2.05 Å, while iron atoms labeled Fe2 exhibit larger Fe—O distances, ranging from 2.03 to 2.22 Å (Table 5). Moreover, the examination of the O—Fe—O angles shows that the Fe2 octahedra are much more distorted than the Fe1 ones, with O—Fe2—O angles (corresponding to adjacent O atoms) ranging from 67 to 112°, whereas the O—Fe1—O angles are between 81 and 105°. The BVS calculations lead to 3+ and 2+ oxidation states for Fe1 and Fe2, respectively.

In the three-dimensional structural framework (Fig. 6*b*), $[\text{Fe2}P_2O_{10}]_\infty$ zigzag ribbons running along the [011] and $[0\bar{1}1]$ directions can be identified; the two chains are oriented 73° to each other. These ribbons drawn in Fig. 7(*a*) are built up from corner-sharing $\text{Fe2}O_6$ octahedra and PO_4 tetrahedra connected to the $\text{Fe2}O_6$ octahedra *via* one edge. The connection between two $[\text{Fe2}P_2O_{10}]_\infty$ zigzag ribbons, running along the directions [011] and $[0\bar{1}1]$, respectively, is illustrated in Fig. 7(*a*): each tetrahedron of one chain shares one corner with an octahedron of the other one. As a consequence, each Fe2 octahedron shares two edges with two other Fe2 octahedra, one edge with one PO_4 tetrahedron, four apices with four other tetrahedra and two apices with two Fe1 octahedra (Fig. 7*b*). The Fe1 octahedron shares its apices with six PO_4 tetrahedra.

Removing from the structure both NH_4^+ and the $[Fe2P_2O_{10}]_\infty$ zigzag ribbons, the ordered part of the real structure is obtained (Fig. 8). Hexagonal tunnels delimited by $Fe1O_6$ octahedra perpendicular to the [011] and $[0\bar{1}1]$ directions can be then shown. Actually, compared with Fig. 6(*b*), twice the number of tunnels running along these directions are observed: in the artificially ordered structure, one half of the hexagonal tunnels was filled by NH_4^+ and the other half by the $[Fe2P_2O_{10}]_\infty$ zigzag ribbons. In the following, the symbols *R* and *N* will be used for the $[Fe2P_2O_{10}]_\infty$ zigzag ribbons and the NH_4^+ species, respectively.

Fig. 8 shows the alignment of the hexagonal tunnels along the **w** direction ($[2\bar{1}1]$). A structural description based on both the stacking and the filling of slices running along **w** can be proposed. The scheme proposed for the ideal β-$NH_4Fe_2(PO_4)_2$ is drawn in Fig. 9(*a*). Each slice exhibits the same *RRNN*, sequence, but a shift corresponding to two hexagons in the **w** direction is observed for adjacent slices. Consequently, a perfect alternation of *R* and *N* is observed in the slices running along $[0\bar{1}1]$.

A comparison of the projection along [011] of the ideal form of β-$NH_4Fe_2(PO_4)_2$ (Fig. 6*b*) with that previously observed for the monoclinic form of α-$NH_4Fe_2(PO_4)_2$ (Fig. 10; Boudin & Lii, 1998) shows close relationships between the two structures. Similar hexagonal tunnels can be also identified; they are filled by either ammonium (*N*) or $[Fe2P_2O_{10}]_\infty$ zigzag ribbons (*R*), but the distribution of these two entities in the tunnels is different in the two structures. Thus, for α-$NH_4Fe_2(PO_4)_2$, the *RNRN* sequence is observed both in the slices running along $\mathbf{b}^\alpha$ {direction equivalent to $[0\bar{1}1]$ in the β-$NH_4Fe_2(PO_4)_2$ form} and the slices running along **w** (direction collinear to $\mathbf{a}_\alpha$; Fig. 9*b*). Consequently, the structure of the α form exhibits a periodicity twice as large as that of the ideal β form ($\sim 2\,a_\beta$) along [210] (Fig. 10).

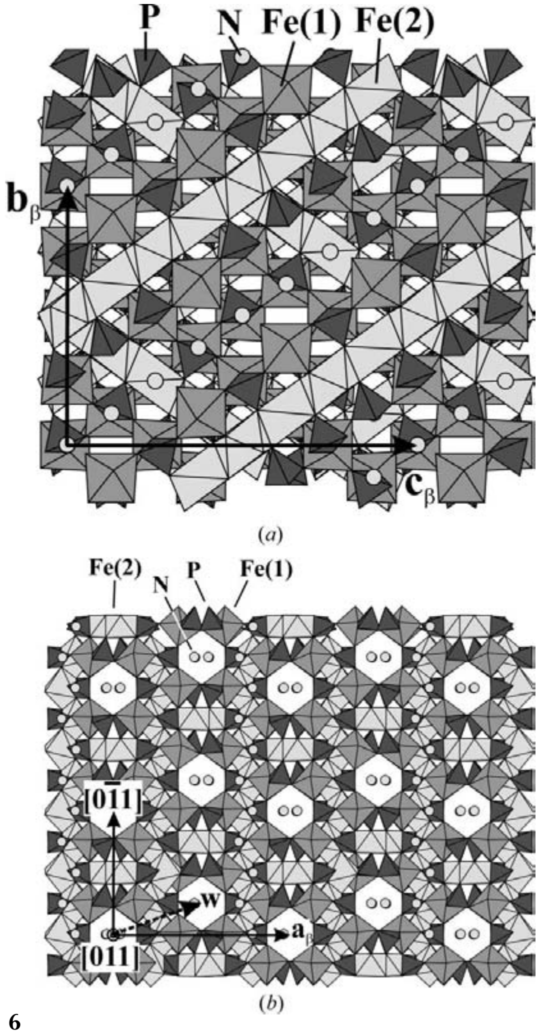

Figure 6
(*a*) Projection of the artificially ordered structure of β-$NH_4Fe_2(PO_4)_2$ along **a**. (*b*) Projection of the artificially ordered structure of β-$NH_4Fe_2(PO_4)_2$ along [011]. Dark-grey tetrahedra, medium-grey and light-grey octahedra correspond to PO_4, $Fe1O_6$ and $Fe2O_6$ polyhedra, respectively.

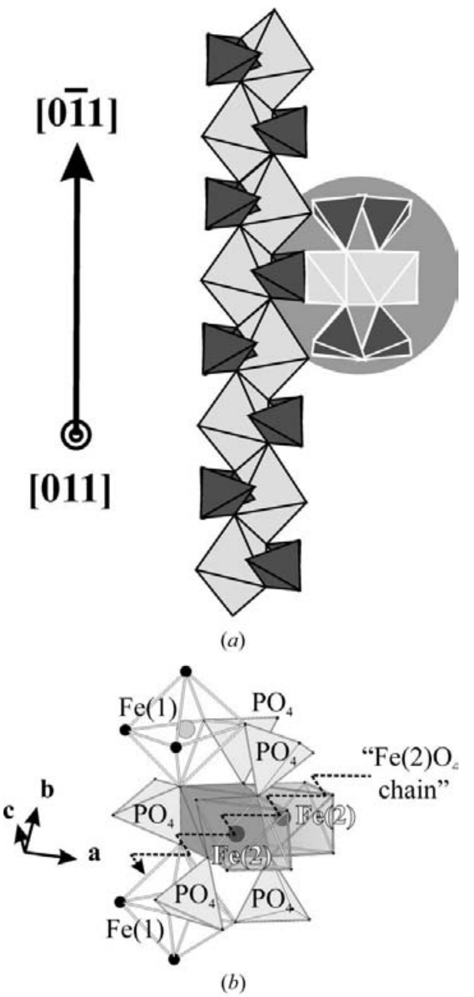

Figure 7
(*a*) View of the $[Fe2P_2O_{10}]_\infty$ zigzag ribbons oriented along [011] and $[01\bar{1}]$ (enlightened by a grey disk) and connection between the two ribbons, (*b*) drawing illustrating the bonding scheme for an $Fe2O_6$ octahedron.

6.3. Further description of the actual structure

The structures of the ideal β form (Fig. 6*a* and Fig. 9*a*) and the ideal α form (Fig. 9*b* and Fig. 10) allow two simple rules to be drawn about the distribution of the NH_4^+ species (*N*) and of $[Fe2P_2O_{10}]_\infty$ ribbons (*R*) in the hexagonal tunnels shown in Fig. 8. The first deals with the fact that tunnels inside the slices running along $[0\bar{1}1]$ (or [011]) are alternately filled with NH_4^+ cations and $[Fe2P_2O_{10}]_\infty$ ribbons, *i.e.* according to the sequence [*NRNR*...]. The second rule concerns the complete absence of constraint to fill tunnels within the slices running along **w**; any *N*/*R* distribution can be envisaged in this direction.

In compliance with these two rules, the ideal α and β forms represent the simplest ordered arrangements of the tunnels that can be observed. The ordering in the ideal form of β-$NH_4Fe_2(PO_4)_2$ (Fig. 6*a* or 9*a*) corresponds to the sequence [*NNRR*...]. In the α form, the ordering along the equivalent direction (Fig. 9*b* or Fig. 10) corresponds to the sequences [*NRNR*...]; this type of ordering corresponds to the smallest periodicity.

In the actual structure of β-$NH_4Fe_2(PO_4)_2$, the diffuse scattering observed on the diffraction patterns is compatible with an ordering in the *bc* plane, but with a loss of correlation along **a** (Fig. 2). Thanks to the second rule, a random distribution of *N* and *R* can be considered within the hexagonal tunnels of the slices running along **w**; the absence of the well defined sequence in the **w** direction is then compatible with a disorder along **a**. Owing to the first rule, all the 'random slices' exhibit the same *N*/*R* sequence along **w**. The resulting perfect *R*/*N* alternation in the $[0\bar{1}1]$ and [011] directions is in agreement with the order observed in the *bc* plane.

The discovery of the actual β-$NH_4Fe_2(PO_4)_2$ form, a disordered form of $NH_4Fe_2(PO_4)_2$, opens the route to the stabilization of new forms. Commensurate or incommensurate modulated distributions, intermediate between the ideal β and

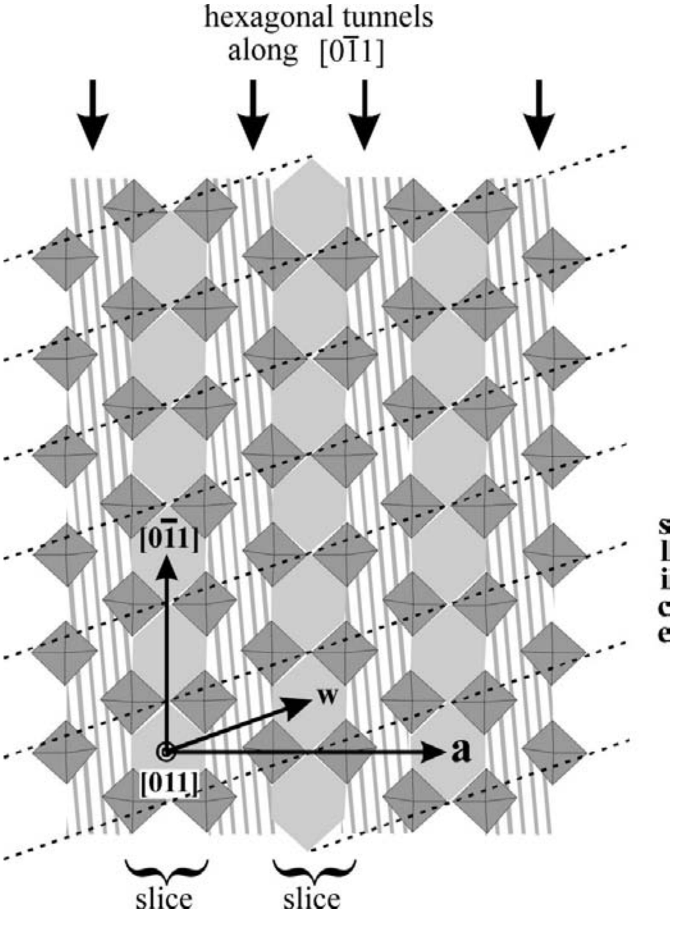

Figure 8
Schematic drawing of $NH_4Fe_2(PO_4)_2$ removing both $[Fe2P_2O_{10}]_\infty$ zigzag ribbons and NH_4^+ species.

Table 5
Interatomic distances (Å).

Fe1–1—O1–1	2.044	Fe1–2—O1–2$^{\rm i}$	2.008
Fe1–1—O1–7$^{\rm i}$	2.028	Fe1–2—O1–6$^{\rm ii}$	2.023
Fe1–1—O2–5$^{\rm iii}$	1.948	Fe1–2—O2–7$^{\rm iv}$	1.997
Fe1–1—O2–6	2.032	Fe1–2—O2–8$^{\rm v}$	1.982
Fe1–1—O2–9$^{\rm vi}$	1.944	Fe1–2—O2–15$^{\rm ii}$	1.9754
Fe1–1—O2–10$^{\rm i}$	2.038	Fe1–2—O2–16$^{\rm vii}$	2.002
Fe1–3—O1–3	2.024	Fe1–4—O1–5$^{\rm viii}$	2.007
Fe1–3—O1–3$^{\rm ix}$	2.024	Fe1–4—O1–5$^{\rm i}$	2.007
Fe1–3—O2–2$^{\rm x}$	1.973	Fe1–4—O2–1$^{\rm xi}$	2.005
Fe1–3—O2–2$^{\rm iii}$	1.973	Fe1–4—O2–1$^{\rm xii}$	2.005
Fe1–3—O2–14$^{\rm vi}$	1.995	Fe1–4—O2–13$^{\rm xiii}$	1.984
Fe1–3—O2–14$^{\rm xiv}$	1.995	Fe1–4—O2–13$^{\rm xv}$	1.984
Fe1–5—O1–4	2.027	Fe1–6—O1–8$^{\rm xvi}$	2.044
Fe1–5—O1–4$^{\rm i}$	2.027	Fe1–6—O1–8$^{\rm vii}$	2.044
Fe1–5—O2–3	2.040	Fe1–6—O2–4	1.941
Fe1–5—O2–3$^{\rm i}$	2.040	Fe1–6—O2–4$^{\rm xvii}$	1.941
Fe1–5—O2–12$^{\rm vi}$	1.951	Fe1–6—O2–11$^{\rm vi}$	2.030
Fe1–5—O2–12$^{\rm xviii}$	1.951	Fe1–6—O2–11$^{\rm xix}$	2.030
Fe2–1—O2–3	2.089	Fe2–2—O2–6$^{\rm xx}$	2.113
Fe2–1—O2–16$^{\rm ii}$	2.185	Fe2–2—O2–14	2.208
Fe2–1—O3–1	2.041	Fe2–2—O3–1$^{\rm i}$	2.201
Fe2–1—O3–2$^{\rm i}$	2.108	Fe2–2—O3–2	2.080
Fe2–1—O3–7$^{\rm ii}$	2.033	Fe2–2—O3–5$^{\rm xix}$	2.120
Fe2–1—O3–8$^{\rm vii}$	2.192	Fe2–2—O3–6$^{\rm vi}$	2.086
Fe2–3—O2–7	2.221	Fe2–4—O2–1$^{\rm xx}$	2.198
Fe2–3—O2–11$^{\rm xiii}$	2.099	Fe2–4—O2–10$^{\rm xxi}$	2.080
Fe2–3—O3–3	2.077	Fe2–4—O3–3$^{\rm i}$	2.110
Fe2–3—O3–4$^{\rm xxi}$	2.201	Fe2–4—O3–4$^{\rm xxi}$	2.043
Fe2–3—O3–5$^{\rm xiii}$	2.089	Fe2–4—O3–7$^{\rm xix}$	2.190
Fe2–3—O3–6$^{\rm xviii}$	2.122	Fe2–4—O3–8$^{\rm vi}$	2.03
P1—O1–4$^{\rm i}$	1.513	P2—O1–3$^{\rm v}$	1.522
P1—O2–1	1.528	P2—O2–4	1.532
P1—O2–10$^{\rm xiii}$	1.564	P2—O2–15$^{\rm ii}$	1.552
P1—O3–1	1.550	P2—O3–2	1.559
P3—O1–2$^{\rm xv}$	1.521	P4—O1–1$^{\rm i}$	1.514
P3—O2–5	1.525	P4—O2–7	1.535
P3—O2–13$^{\rm xiii}$	1.550	P4—O2–11$^{\rm xiii}$	1.567
P3—O3–3	1.566	P4—O3–4	1.543
P5—O1–8$^{\rm xxi}$	1.519	P6—O1–7$^{\rm xxi}$	1.518
P5—O2–2$^{\rm xxi}$	1.563	P6—O2–8$^{\rm xx}$	1.560
P5—O2–9	1.527	P6—O2–12	1.520
P5—O3–5	1.557	P6—O3–6	1.564
P7—O1–6$^{\rm xxi}$	1.517	P8—O1–5$^{\rm xxi}$	1.516
P7—O2–6$^{\rm xx}$	1.556	P8—O2–3$^{\rm xxi}$	1.553
P7—O2–14	1.539	P8—O2–16	1.533
P7—O3–7	1.544	P8—O3–8	1.552

Symmetry codes: (i) $\frac{1}{2}-x, 1-y, z$; (ii) $-\frac{1}{2}+x, 1-y, -z$; (iii) $-x, -\frac{1}{2}+y, \frac{1}{2}-z$; (iv) $x, -\frac{1}{2}+y, -\frac{1}{2}+z$; (v) $\frac{1}{2}-x, \frac{1}{2}-y, -\frac{1}{2}+z$; (vi) $-\frac{1}{2}+x, \frac{1}{2}-y, \frac{1}{2}-z$; (vii) $1-x, y, -z$; (viii) $-\frac{1}{2}+x, 1-y, 1-z$; (ix) $-x, y, 1-z$; (x) $x, -\frac{1}{2}+y, \frac{1}{2}+z$; (xi) $x, \frac{1}{2}+y, \frac{1}{2}+z$; (xii) $-x, \frac{1}{2}+y, \frac{1}{2}-z$; (xiii) $-\frac{1}{2}+x, \frac{3}{2}-y, \frac{1}{2}-z$; (xiv) $\frac{1}{2}-x, \frac{1}{2}-y, \frac{1}{2}+z$; (xv) $\frac{1}{2}-x, \frac{3}{2}-y, \frac{1}{2}+z$; (xvi) $-\frac{1}{2}+x, -y, -z$; (xvii) $\frac{1}{2}-x, -y, z$; (xviii) $1-x, \frac{1}{2}+y, \frac{1}{2}-z$; (xix) $1-x, -\frac{1}{2}+y, \frac{1}{2}-z$; (xx) $\frac{1}{2}+x, \frac{1}{2}-y, \frac{1}{2}-z$; (xxi) $\frac{1}{2}-x, 2-y, z$.

α forms can also be expected: numerous polytypes could then be generated by the filling mechanism of the tunnels in the slices oriented along **w**. The energy of these materials may be close to each other, so that the experimental conditions for the synthesis of these phases are suspected to play a crucial role. It is most probable that the perfectly ordered structure of α-$NH_4Fe_2(PO_4)_2$ may have been stabilized by the high-temperature, high-pressure, hydrothermal synthesis conditions. This suggests that it should be possible to synthesize numerous other forms of $NH_4Fe_2(PO_4)_2$ by modifying the experimental conditions, or by chemical substitution or doping. Moreover, new ordering in the *bc* plane should be generated by changing the Fe/NH_4^+ ratio.

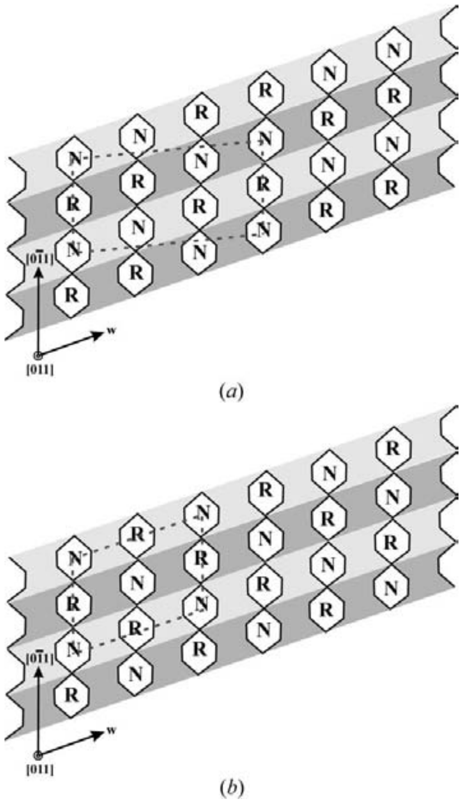

Figure 9
Modelling of the filling of the slices running along **w** for the ideal β-$NH_4Fe_2(PO_4)_2$ (*a*) and for the α-$(NH_4)Fe_2(PO_4)_2$ (*b*).

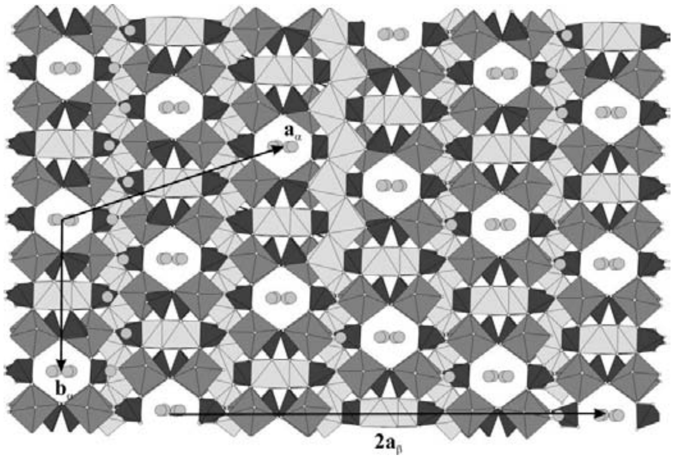

Figure 10
Projection of the monoclinic ordered structure of α-$(NH_4)[Fe_2(PO_4)_2]$ along $\bar1\bar1\bar2$.

7. Concluding remarks

Single-crystal X-ray diffraction always occupies a central position in the structural investigations of new materials. Over the last few years, the systematic use of two-dimensional detectors has led to the increasingly frequent observation of complex diffraction phenomena such as aperiodicity or diffuse scattering. The development of the superspace formalism (Janssen *et al.*, 1999) allowed an accurate determination of the aperiodic structures. The understanding of disorders associated with the diffuse scattering is more difficult. The classical approach considers only the long-range-order coherent part of the diffraction pattern and leads to an average structure of the material. However, diffuse scattering phenomena are related to short-range order. The real structure of the material is then somewhere between the average structure and an ideal perfectly ordered structure. For this purpose and following symmetry considerations, an ideal diffraction pattern has been designed for β-$NH_4Fe_2(PO_4)_2$ by replacing the diffuse scattering, observed in the real reciprocal space, by point reflections. A partial integration of the diffuse lines from the experimental frames allows us to assign intensities to these additional reflections. The superspace formalism is then very useful for a modelling of this pseudo-long-range order; it allows the building of a model step-by-step and improves the convergence by reducing the number of refinement parameters. The structure of the perfectly ordered material leads to a peculiar NH_4^+/Fe order for β-$NH_4Fe_2(PO_4)_2$. Finally, this structure gives an insight into the local order of the real structure.

References

Ai, M. & Ohdan, K. (1997). *Appl. Catal. A*, **150**, 13–20.
Ai, M. & Ohdan, K. (2000). *J. Mol. Catal. A Chem.* **159**, 19–24.
Becker, P. J. & Coppens, P. (1974). *Acta Cryst.* A**30**, 129–153.
Bonhomme, F., Thoma, S. G. & Nenoff, T. M. (2002). *Microporous Mesoporous Mater.* **53**, 87–96.
Boudin, S. & Lii, K.-W. (1998). *Inorg. Chem.* **37**, 799–803.
Burla, M., Camalli, M., Carrozzini, B., Cascarano, G. L., Giacovazzo, C., Polidori, G. & Spagna, R. (2002). *SIR*2002. Institute of Crystallography, Bari, Italy.
Cavellec, M., Riou, D. & Férey, G. (1994). *Acta Cryst.* C**50**, 1379–1381.
Chung, S. Y., Bloking, J. T. & Chiang, Y. M. (2002). *Nat. Mater.* **1**, 123–128.
Daturi, M., Busca, G., Guesdon, A. & Borel, M. M. (2001). *J. Mater. Chem.* **11**, 1726–1731.
Duisenberg, A., Kroon-Batenburg, L. & Shreurs, A. (2003). *J. Appl. Cryst.* **36**, 220–229.
Elkaïm, E., Berar, J. F., Gleitzer, C., Malaman, B., Ijjaali, M. & Lecomte, C. (1996). *Acta Cryst.* B**52**, 428–431.
Ijjaali, M., Malaman, B., Gleitzer, C., Warner, J. K., Hriljac, J. A. & Cheetham, A. K. (1990). *J. Solid State Chem.* **86**, 195–205.

Janssen, T., Janner, A., Looijenga, A. & de Wolff, P. M. (1999). *International Tables for Crystallography*, Vol. C, 2nd Ed., pp. 899–937. Dordrecht: Kluwer Academic Publishers.

Krasnikov, V. V., Constant, Z. A. & Fundamenski, V. S. (1983). *Isvestya Akad. Nauk. SSSR Neorg. Mater.* **19**, 1373–1378.

Modaressi, A., Courtois, A., Gérardin, R., Malaman, B. & Gleitzer, C. (1981). *J. Solid State Chem.* **40**, 301–311.

Moore, P. B. & Araki, T. (1979). *Am. Mineral.* **64**, 587–592.

Padhi, A. K., Nanjundaswamy, K. S. & Goodenough, J. B. (1997). *J. Electrochem. Soc.* **144**, 1188–1194.

Petricek, V. & Dusek, M. (2000). *JANA*2000. Institute of Physics, Praha, Czech Republic.

Prosini, P. P., Lisis, M., Scaccia, S., Carewska, M., Cardelline, F. & Pasquali, M. (2002). *J. Electrochem. Soc.* **149**, A297–A301.

Schmid-Beurmann, P. (2000). *J. Solid State Chem.* **153**, 237–247.

Sheldrick, G. M. (1997). *SADABS*. University of Göttingen, Germany.

Song, Y., Yang, S., Zavalig, P. Y. & Whittingham, M. S. (2002). *Mater. Res. Bull.* **37**, 1249–1257.

Wolff, P. M. de, Janssen, T. & Janner, A. (1981). *Acta Cryst.* A**37**, 625–636.

Zecchina, A., Marchese, L., Bordiga, S., Pazé, C. & Gianotti, E. (1997). *J. Phys. Chem. B*, **101**, 10128–10135.